Influence of anatomical features of different brain regions on the spatial localization of fiber photometry signals

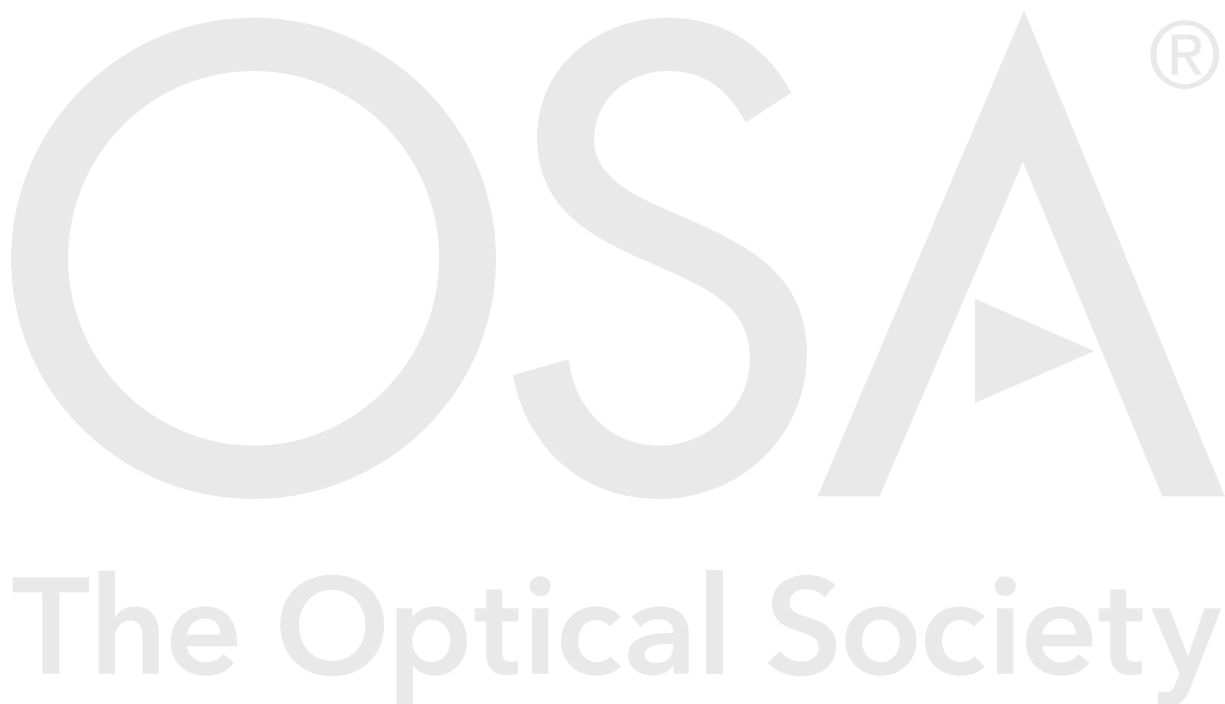CINZIA MONTINARO[1,2,*], MARCO PISANELLO[1], MARCO BIANCO[1,3], BARBARA SPAGNOLO[1], FILIPPO PISANO[1], ANTONIO BALENA[1], FRANCESCO DE NUCCIO[2], DARIO DOMENICO LOFRUMENTO[2], TIZIANO VERRI[2], MASSIMO DE VITTORIO[1,3,4,+], FERRUCCIO PISANELLO[1, 5,+]

[1]*Istituto Italiano di Tecnologia (IIT), Center for Biomolecular Nanotechnologies, Via Barsanti 14, 73010 Arnesano (Lecce), Italy*
[2]*Dipartimento di Scienze e Tecnologie Biologiche e Ambientali, Università del Salento, Via per Monteroni, 73100 Lecce, Italy*
[3]*Dipartimento di Ingegneria dell'Innovazione, Università del Salento, Via per Monteroni, 73100 Lecce, Italy*
[+]*Equaly contributing authors*
[4] *massimo.devittorio@iit.it*
[5] *ferruccio.pisanello@iit.it*
[*] *cinzia.montinaro@iit.it*

Abstract: Fiber photometry is widely used in neuroscience labs for *in vivo* detection of functional fluorescence from optical indicators of neuronal activity with a simple optical fiber. The fiber is commonly placed next to the region of interest to both excite and collect the fluorescence signal. However, the path of both excitation and fluorescence photons is altered by the uneven optical properties of the brain, due to local variation of the refractive index, different cellular types, densities and shapes. Nonetheless, the effect of the local anatomy on the actual shape and extent of the volume of tissue that interfaces with the fiber has received little attention so far. To fill this gap, we measured the size and shape of fiber photometry efficiency field in the primary motor and somatosensory cortex, in the hippocampus and in the striatum of the mouse brain, highlighting how their substructures determine the detected signal and the depth at which photons can be mined. Importantly, we show that the information on the spatial expression of the fluorescent probes alone is not sufficient to account for the contribution of local subregions to the overall collected signal, and it must be combined with the optical properties of the tissue adjacent to the fiber tip.

1. Introduction

The development of high-efficiency optical indicators of neural activity has widened the application of fiber photometry (FP) [1–4], a method employing flat-cleaved step-index optical fibers (OFs) to monitor time-dependent functional fluorescence and/or lifetime variations related to several physiological phenomena, including calcium (Ca^{2+}) levels [5], membrane potential [6], neurotransmitters' transients [7] and the intracellular biochemical state of neurons [8]. The OF is commonly placed next to the region of interest and used to excite the fluorescent indicators and to collect the resulting functional signal. The brain volume contributing to the overall signal depends on the constitutive parameters of the OF, including numerical aperture (NA), core/cladding dimensions and refractive index [9], and it is the result of the combination of the three-dimensional excitation and collection fields [9–12]. Moreover, both excitation and fluorescence photons undergo tissue attenuation and scattering, and the generated fluorescence strongly depends on: (i) how the excitation light distributes at the output of the OF, and (ii) how many fluorescence photons generated in a specific point reach the fiber facet.

47   While different methods exist to estimate the FP sensitivity volume in brain tissue [9,13],
48   the optical properties of the brain are highly uneven, not only at the cellular and subcellular
49   level, but also on the scale of hundreds of micrometers and millimeters. The anatomical
50   distribution of cells bodies, for instance, significantly varies across different brain regions, and
51   distinct structures are characterized by a different cell density, while others contain mostly
52   neuropil. In this regard, representative examples can be identified in the cerebral cortex (CTX),
53   the hippocampus (HP) and the striatum (STR) of the mouse brain. The CTX has a columnar
54   structure consisting of six alternating layers (LI-LVI) [14], each one with a specific anatomy
55   characterized by different cellular densities and cell types. In addition, the depth of each layer
56   and its composition depends on the specific subregion, with peculiar known differences across
57   motor, somatosensory, associative and visual cortex [15]. Similarly, the HP has a layered
58   structure too, with neural bodies mainly concentrated along a curve, from *Cornu Ammonis* 1
59   (CA1) through *Cornu Ammonis* 4 (CA4) [16,17], with basal and apical dendrites extending in
60   two different directions and generating highly fibrous regions above and below the cell bodies
61   layers. The STR organization follows, instead, a spatio-molecular code and the striatal circuitry
62   can be divided into two major pathways of striatal projection neurons (SPNs) that have distinct
63   neuroanatomical and molecular features [18,19]. Therefore, the anatomy of cellular shapes and
64   their distribution adds an additional layer of complexity to the problem of estimating the spatial
65   localization of FP signal. At the same time, the use of genetically encoded fluorescent indicators
66   of neural activity makes a subpopulation of cells act as source of functional fluorescence, while
67   non-tagged neurons influence the collected signal as a passive optical medium, defining the
68   optical properties of the tissue.
69   In this study we report how the shape and size of the three-dimensional fiber photometry
70   efficiency field changes across the cortex, hippocampus and striatum of the mouse brain. We
71   used the widely adopted *Thy1*-GCaMP6 line [20,21]. This strain is characterized by GCaMP
72   expression under the *Thy1* promoter, an immunoglobulin superfamily expressed by projection
73   neurons, allowing for identifying neuronal somata and projections across different brain areas
74   [22–24]. Importantly, we relate the measured FP efficiency fields to the local cytoarchitecture
75   specific of the investigated regions, highlighting significant intra-region differences. In this
76   framework, our results suggest that fiber photometry data should be analyzed by considering
77   the specific region from which the collected signal is generated, since each peculiar substructure
78   contributes in defining the final sensitivity volume in terms of both size and shape.

79   **2. Results**

80   *2.1 Optical Setup and Methodology*

81   A two-photon (2P) laser scanning system, displayed in *Figure 1A*, was used to measure the
82   illumination (*β*) and collection (*η*) fields [9] of an OF stub with NA = 0.39 and core diameter
83   of 200 μm, positioned next to the region of interest on 300 μm-thick coronal brain slices
84   obtained from *Thy1*-GCaMP6*s* transgenic mice (see *right* inset *Figure 1A*). As the slice is only
85   100 μm thicker than the fiber core, a correct placement of this latter at the center of the slice
86   along z was achieved using a micromanipulator with resolution of ~0.1 μm (Scientifica
87   PatchStar stepper motor micromanipulator). A fs-pulsed near-infrared (NIR) laser beam (λ_{ex} =
88   920 nm) was used to generate a fluorescent voxel scanned in three dimensions close to the facet
89   of the fiber, in a z-stack spanning 100 μm across the fiber facet (z step 10 μm). Resulting
90   fluorescence was detected by a photomultiplier tube ("*μscope* PMT", *μ*) in non-descanned
91   epifluorescence configuration, and simultaneously a fraction of the signal was collected by the
92   optical fiber and guided to a second PMT ("*fiber* PMT", *f*). This generated two image stacks
93   *μ(x,y,z)* and *f(x,y,z)*, respectively. The OF's collection efficiency field was then computed as
94    $\eta(x,y,z)= f(x,y,z)/\mu(x,y,z)$ [9]. The same system was employed to measure the normalized
95   excitation field *β(x,y)* in the same brain region by delivering a 473 nm continuous wave (CW)
96   laser beam through the same fiber and collecting the resulting fluorescence signal with a
97   sCMOS camera. Since the depth of focus of the employed objective (Olympus XLFLUOR-340

98 4x/NA 0.28) was estimated to be 57 µm (Nikon's MicroscopyU, 2021), β was acquired as a
99 single slice. To match η to β, the average projection on six slices of $\eta(x,y,z)$ (equivalent to a
100 thickness of 60 µm) was performed, resulting in the 2D field $\eta(x,y)$. The photometry efficiency
101 field was then retrieved as $\rho(x,y)= \eta(x,y)\cdot\beta(x,y)$ [9,13]. This overall procedure is summarized in
102 *Figure 1B*. The slice thickness of 300 µm was chosen considering the tradeoff between: (i) the
103 influence of the slice thickness on the recorded fields and (ii) the ability to detect fluorescence
104 photons with the microscope objective while delivering light through the fiber to measure $\beta(x,y)$
105 (e.g. if the slice is too thick $\beta(x,y)$ is not visualized properly and scattering does not allow to
106 then reconstruct $\rho(x,y)$).
107 $\rho(x,y)$ therefore takes into account the optical fiber's constitutive parameters and the properties
108 of the brain tissue (e.g. refractive index, absorption and scattering coefficients) interposed
109 between the light source and the OF [9,26]. We employed ρ as main figure of merit to evaluate
110 the dependence of the FP signal in the different regions investigated in this work. *Figure 1C*
111 *(top)* shows representative coronal brain slices obtained from *Thy1*-GCaMP6*s* transgenic mice
112 highlighting the specific brain regions investigated in this work, together with their two-photon
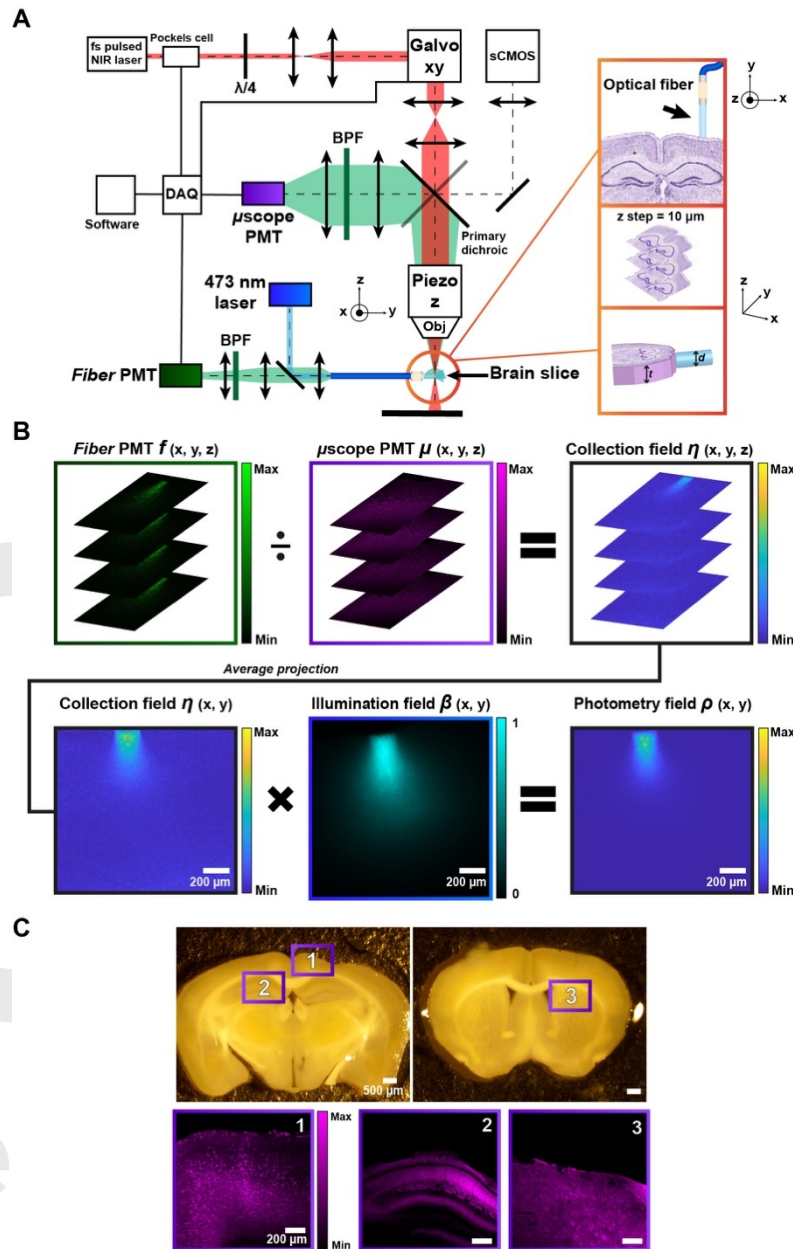113 microscope images *(bottom)*.
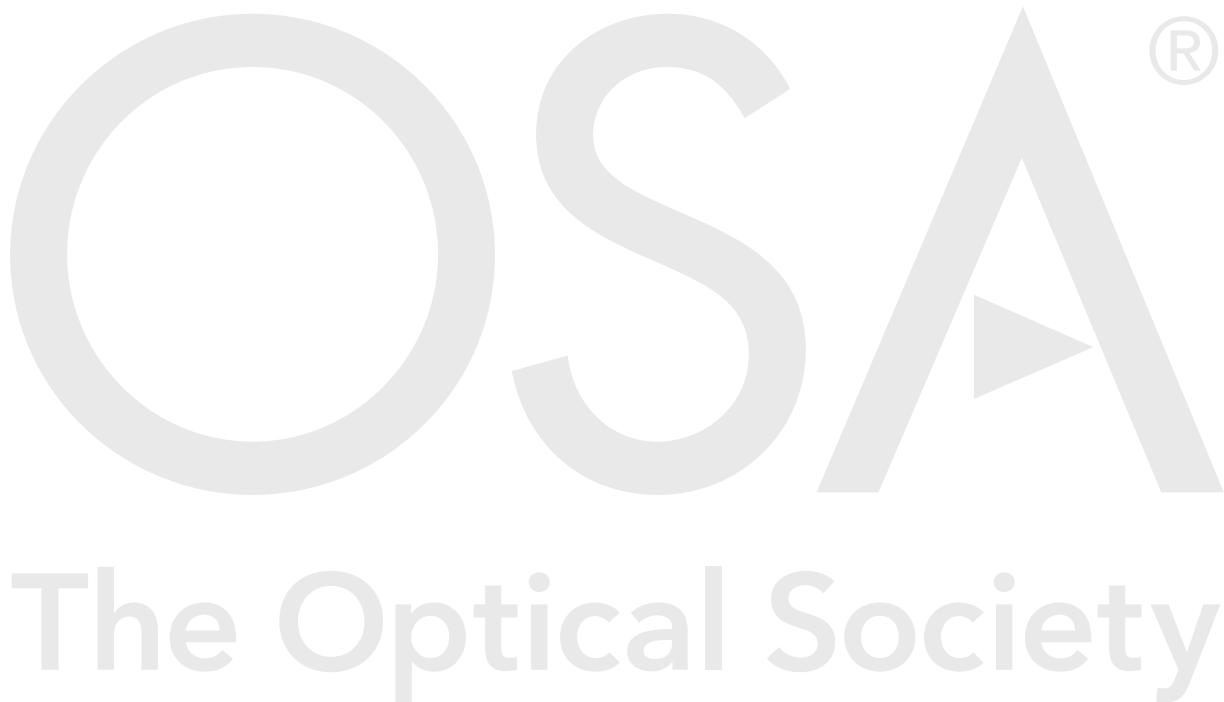
Fig. 1. (A) (*left*) Setup used to measure the collection η and illumination β fields, (*right*) zoom of an optical fiber placed next to the brain region of interest (top), schematic representation of z-stack (middle) and the fiber placement at the center of the slice along z (bottom). In the bottom sketch, $t=300\mu m$ represents the slice thickness and $d=200$ µm represents the fiber core diameter, which is placed at the center for the slice along z. Zooms are not shown in scale. (B) Schematic representation of the combination of $\eta(x,y)$ and $\beta(x,y)$ to obtain $\rho(x,y)$. (C) (*top*) Stereomicroscope images of coronal brain slices obtained from *Thy1*-GCaMP6s transgenic mice, (*bottom*) two-photon microscope images of the brain regions: (1) CTX, (2) HP, (3) STR. The boxes' colors (magenta, green and blue) in (B) and in (C) correspond to the detectors, shown in (A).

127   *2.2 Comparing Photometry Efficiency Fields across CTX, HP and STR*

128   To identify the influence of anatomical features on the spatial behavior of FP signals, we have
129   chosen to investigate light collection volumes of optical fibers placed next to the mouse cerebral
130   cortex, the hippocampus and the striatum, which are characterized by intrinsically different
131   cytoarchitecture.
132   The cerebral cortex can be divided in different areas: motor, somatosensory, visual and
133   auditory, each of which has its own function and organization. All the neocortical areas derived
134   from a six-layered structure where the term layer refers to an aggregate of neuronal cell bodies
135   and/or neuropil. As a particular case, primary motor cortex (M1) lacks LIV, consisting of
136   granular cells [14]. Moreover, the cerebral cortex shrinks into a single S-shaped layer to
137   constitute the hippocampus, in which, however, the subdivision into substructures continues,
138   distinguishing CA1, CA2, CA3 and CA4 areas [17]. The main output connections of the
139   hippocampus are represented by the pyramidal neurons of the CA1, innervating numerous areas
140   of the brain, with a non-homogeneous cell typology. CA1 pyramidal neurons can be
141   differentiated according to their size, shape and location of their soma, or to basal and apical
142   dendritic arborizations and specializations [27]. On the contrary, striatum cellular organization
143   appears to be more homogeneous, but it presents a peculiar distribution into patch and matrix
144   compartments and in two main pathways, formed by subtypes of striatal projection neurons
145   (SPN) having different molecular identities, and featuring a subdivision based on a spatio-
146   molecular code [19].
147   *Figure 2A* shows representative results of f and β measured for a 0.39 NA OF placed next
148   to M1, CA1 and dorsal STR, together with a reference 2P fluorescence image. In the case of
149   M1 (*Figure 2A*, *left column*), both collection and excitation fields extend up to LV, with some
150   signal arising also from LVI, with decreasing intensity as a function of depth. However, the
151   photometry efficiency field ρ has shorter extension in depth with respect to η and β, being the
152   product between the two. This is shown in *Figure 2B, top*, showing iso-intensity lines at 10%,
153   20%, 40%, 60% and 80% of the maximum number of collected photons on the photometry
154   field, together with their 3D representation in a rotationally symmetric diagram (*Figure 2B*,
155   *bottom*). Isolines in *Figure 2B top* have a narrow and elongated shape with: isolines at 80% and
156   60% extending at the boundary between LI and LII-III, isolines at 40% that do not exceed the
157   depth of LII-III, and isolines at 20% and 10% that reach up to LV. In HP (*Figure 2A-B*, *central
158   column*), the isolines clearly follow the anatomical structure of CA1 with a two-lobe shape:
159   isolines from 80% to 40% outline the basal dendrites, while 20% and 10% isolines reach the
160   apical dendrites layer and slightly narrow across the cell bodies of pyramidal neurons. In STR,
161   instead, no clear anatomy-dependent collection is observed, while the spatial behavior of the
162   photometry efficiency field results to be distributed more homogeneously.
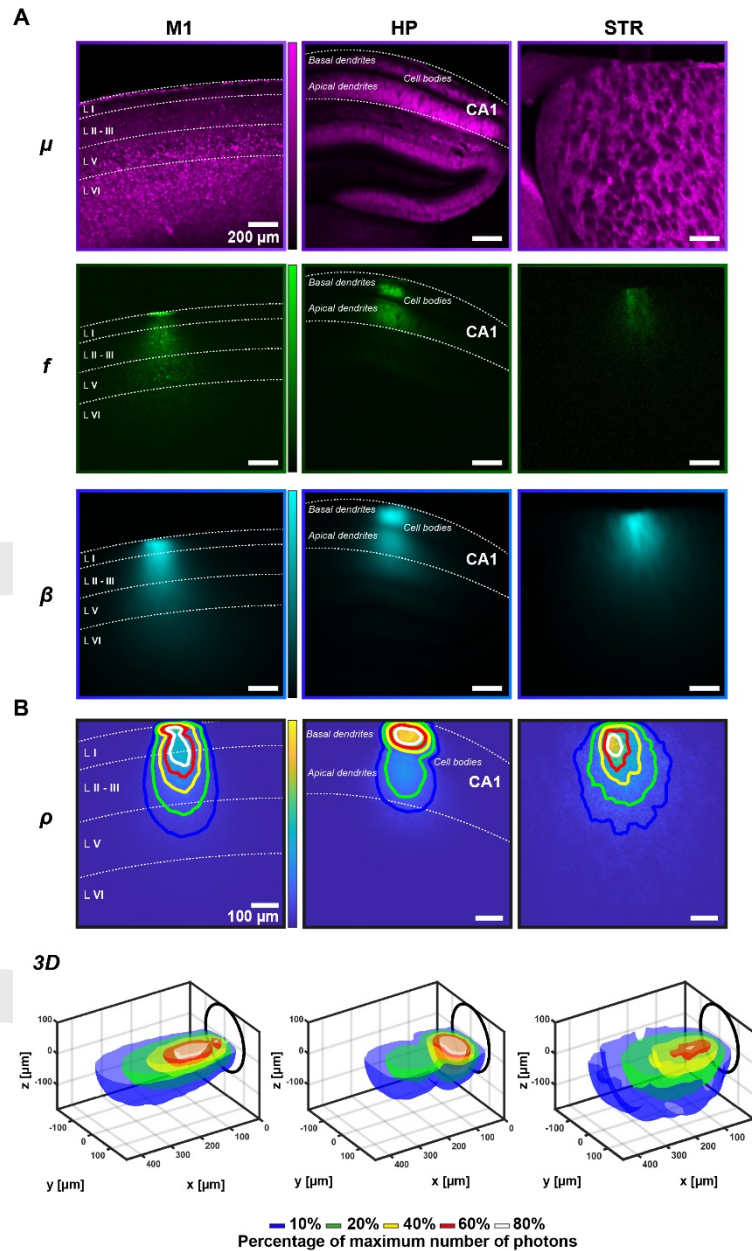
Fig. 2. (A) Representative *μscope* PMT image (*top*), *fiber* PMT image (*middle*) and the illumination field (*bottom*) of primary motor cerebral cortex (*left*), hippocampus (*center*) and striatum (*right*). Scalebar in all the panels (A) is 200 μm. (B) *(top)* Photometry collection efficiency field for each region with comparison of iso-intensity surfaces at 10%, 20%, 40%, 60%, and 80% of the maximum number of photons are shown (in blue, green, yellow, red, white respectively); *(bottom)* their 3D configuration as surfaces of revolution obtained by rotating the isolines around the fiber axis. Scalebar in all the panels (B) *(top)* is 100 μm. Images of *μ* and *f* in panel (A) were adjusted for visualization's sake.

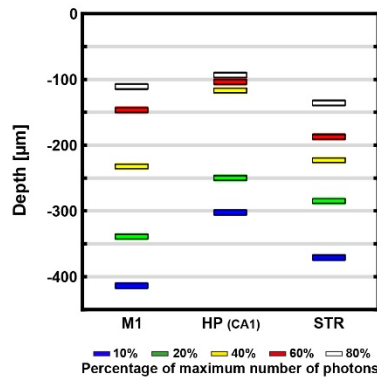The difference between the detection depths at the different contribution percentages is quantified in *Figure 3A*: each horizontal line represents the maximum depth $d_{region}^{percentage}$ reached by a specific iso-intensity surface. The blue data points, relative to $d_{region}^{10\%}$, clearly

175 show that the photometry efficiency field extends deeper for M1 and STR with respect to HP (
176 $d_{M1}^{10\%} = 414 \pm 9 \,\mu m$, $d_{STR}^{10\%} = 371 \pm 45 \,\mu m$ and $d_{HP}^{10\%} = 302 \pm 24 \,\mu m$, mean ± standard
177 deviation on n = 3, single measures reported in *Supplementary Figures 1-3*). Another peculiar
178 difference is that in the HP the high intensity region (see white, red and yellow lines) is confined
179 above a depth of ~117 µm, while for M1 and STR it is more evenly distributed until ~232 µm
180 and ~223 µm respectively (see the spacing between red, yellow and white data points in *Figure*
181 *3A*).
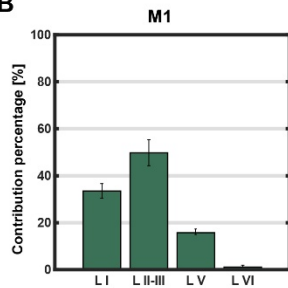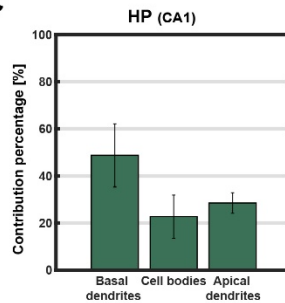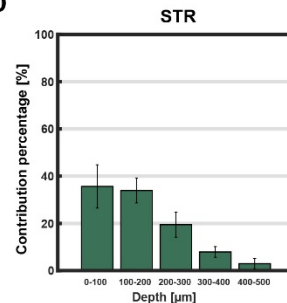
182

183 Fig. 3. (A) Detection depths at the different contribution percentages between M1, HP and STR.
184 Each bar indicates the different contribution of each anatomical feature in (B) M1, (C) CA1
185 subcellular organization reveals three different areas contributing to the overall photometry
186 signal: basal dendrites, cell bodies and apical dendrites and (D) STR. Error bars in bar graphs in
187 panels (B), (C) and (D) represent the standard deviation of the percentages evaluated on N = 3
188 brain slices.

189   On these bases, we have estimated how much each anatomical and cellular feature
190 contributes to the collected signal. This is reported in *Figure 3B* and *C* for M1 and HP. In the
191 case of M1 roughly half of the signal is recorded from LII-III, despite GCaMP is mostly
192 expressed by LV pyramidal neurons [27]. Therefore, when the fiber is placed at the cortex
193 surface, the collected fluorescence is mostly generated by the apical dendrites extending from
194 LV's soma to LII-III and LI, which together account for ~80% of the overall collected photons
195 against the ~16% assigned to LV. In HP instead (*Figure 3C*) the fluorescence signal generated
196 in CA1 has a peculiar sub-distribution: ~49% derives from the top layer constituted by basal
197 dendrites, ~23% from pyramidal cell layer and the remaining ~28% can be ascribed to the apical
198 dendrites region. The striatum is instead macroscopically more uniform, and its microscopic
199 anatomy is concealed by histochemical cells organization in striosomes (or patches) and matrix
200 compartments. Indeed, STR has a non-layered cytoarchitecture and in addition it receives
201 several afferent fibers from cortical and subcortical structure and projects efferent fibers to
202 basal ganglia nuclei [28]. These results in a homogeneous propagation of photons, and the
203 spatial distribution of photometry efficiency can hardly be related to specific anatomical

204 features. Instead, it is interesting to analyze it as a function of depth, as clearly highlighted in
205 the progressive signal decrease in the bar graph in *Figure 3D*.

206 *2.3 Variability of Photometry Efficiency Field across Motor and Somatosensory Cortex*

207 The measurements described in Section 2.2 suggest that the different anatomy of functional
208 brain structures influences the shape of the photometry efficiency field, as well as the maximum
209 depth at which the signal is collected; therefore, we expect that also anatomical differences
210 within the same region strongly affect the spatial behavior of ρ. A representative example is the
211 presence of LIV in somatosensory cortex (S1), which is instead missing in M1. To analyze this,
212 we have chosen a coronal section at -0.10 mm anterior-posterior (A.P.) from B*regma* and
213 positioned the OF next to M1 or S1 (*Figure 4A*). Obtained *f* and *β* fields are shown in *Figure*
214 *4B* for two nominally identical slices from two different mice, while the ρ field is displayed in
215 *Figure 4C*, with the iso-surfaces overlaid and their 3D configuration.

216
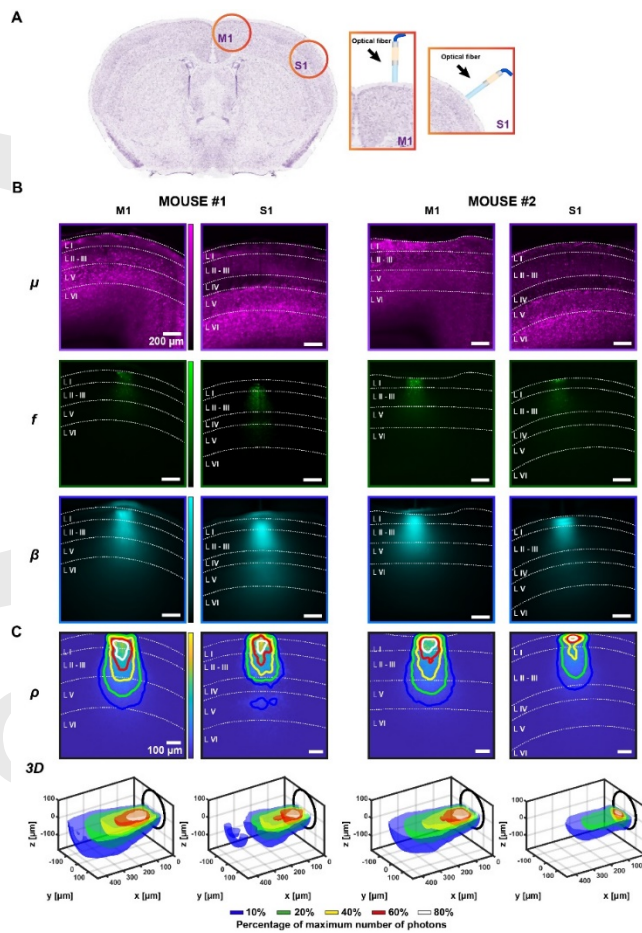
217 Fig. 4. (A) (*left*) Schematic representation of coronal brain slice at -0.10 mm anterior-posterior
218 from B*regma*, (*right*) the optical fiber positioned next to M1 or S1. Brain slice and optical fibers
219 are not shown in scale. (B) Representative *μscope* PMT image (*top*), *fiber* PMT image (*middle*)
220 and illumination field (*bottom*) of M1 and S1 for mouse#1 and mouse#2. Scalebar in all the
221 panels (B**)** is 200 μm. (C) (*top*) Photometry collection efficiency field for each region with
222 comparison of iso-intensity surfaces at 10%, 20%, 40%, 60%, and 80% of the maximum number
223 of photons are shown (in blue, green, yellow, red, white respectively), *(bottom)* their 3D
224 configuration as surfaces of revolution obtained by rotating the isolines around the fiber axis.
225 Scalebar in all the panels (C) (*top*) is 100 μm. Images of *μ* and *f* in panel (A) were adjusted for
226 visualization's sake.

227   In this specific area of M1 the 10% intensity line reaches LV, which accounts for about the
228   ~11% of the overall collected signal (see bar graphs in *Figure 5A*), while for LI and LII-III we
229   have found this value to be ~30% and ~60%, respectively. In S1, instead, the 10% isoline stops
230   across the boundary between LII-III and LIV, resulting in a strong reduction (~36%) of the
231   influence of LV on the collected fluorescence, which accounts for the ~7% of the overall
232   fluorescence. The main contribution derives instead from LI and LII-III, which together
233   generate more than the 80% of the photometry field signal. In *Thy1*-GCaMP6 transgenic line,
234   LIV cell bodies do not express GCaMP6 [27], pyramidal neurons are smaller [29] and do not
235   show a dendritic arborization toward LI and LII-III, with respect to typical LV pyramidal
236   neurons [30]. Therefore, LIV acts as a shield for optical signal from deeper regions, and its
237   thickness influences the ability to collect fluorescence from LV. This is shown by a comparison
238   by 10% iso-intensity collection lines from S1 in mouse #2 and #1, with this latter showing some
239   signal emerging from LV. A more detailed analysis of LIV thickness, displayed in *Figure 5B*,
240   shows that LIV is slightly thinner (~20 μm) in mouse #1, enabling more signal to reach the
241   fiber facet from LV with respect to mouse #2.
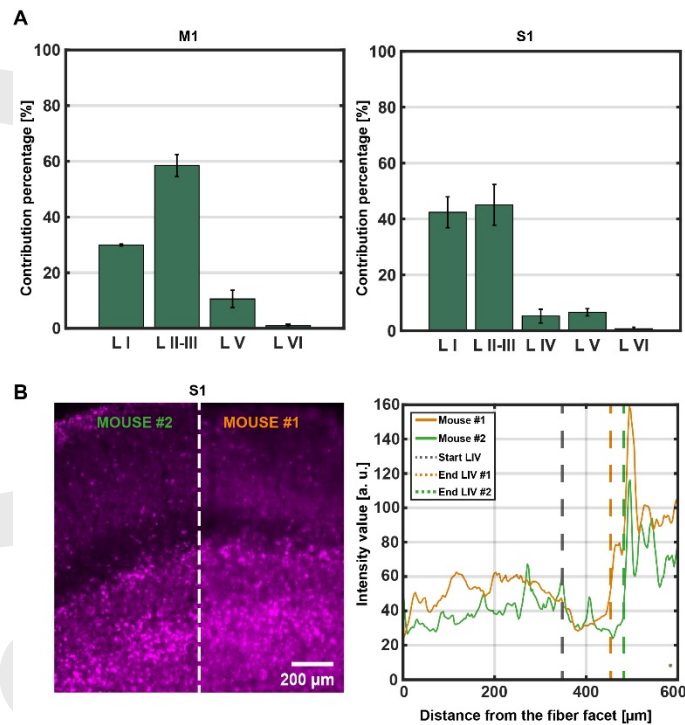
243   Fig. 5. (A) Anatomical feature contributes for M1 and S1. (B) S1 microscopy images side-by-
244   side with the thickness profile of Layer IV for mouse#1 with respect to mouse#2. Error bars in
245   bar graphs in panels (A) represent the standard deviation of the percentages evaluated on N = 2
246   brain slices.

3.   Discussion and Conclusion

248   As fiber photometry is widely employed for collecting functional fluorescence from the mouse
249   brain in free-moving animals, the definition of the collection volume was so far mainly based
250   on (i) the distribution of the functional fluorescence in the targeted subpopulation of cells, (ii)
251   the collection properties of the employed device, (iii) the properties of scattering in brain tissue.
252   These latter can be modeled by the *Henyey–Greenstein* scattering model, based on the main
253   parameters of scattering lengths ($1/\mu_s$), absorption coefficient (μ_a) and anisotropy (g). μ_s, μ_a and
254   g have all been observed to vary across different brain regions and as a function of the

255   wavelength [31], and their influence on the collection volume can be estimated by ray tracing
256   methods [9]. However, these approaches are based on the hypothesis that these parameters are
257   uniform in the probed region of interest.
258   We here report the evidence that an additional layer of complexity related to the specific
259   anatomical features of the targeted brain structures and substructures has to be considered. The
260   cytoarchitecture of different brain regions is crucial in defining the shape and the size of the
261   light collection volume and, therefore, the type and number of cells contributing to the recorded
262   signal. This is clearly shown in *Figure 3* for the transgenic mouse line *Thy1*-GCaMP6*s*,
263   highlighting that the anatomy of the brain region under investigation directly influences the
264   depth at which fluorescence is collected. Indeed, in M1, S1 and HP the thickness of the different
265   layers set constrains or favors the ability to mine signal below a depth of 300 μm (*Figure 3A-*
266   *C*, *Figure 4*). On the contrary, structures with more uniform cell distribution at the millimeters
267   scale, which likely results in uniform scattering parameters, like the striatum, show an even
268   decrease of signal intensity as a function of depth (*Figure 3D*).
269   Overall, this is the consequence of the heterogeneous optical properties of the brain, which
270   are due to different cellular types, densities and shapes, different scattering and attenuation
271   coefficients, and to local variations of the refractive index, which can also generate unexpected
272   reflection and distortions when light travels across multiple regions [32,33]. On this respect,
273   even small differences across multiple mice could result in detectable light collection
274   differences and influence the experimental statistics, as observed in the comparison for S1 in
275   two different animals (*Figure 4* and *5)* where a small difference in thickness of LIV affects
276   light collection efficiency from LV. Although this is not presented in a statistical fashion, the
277   two investigated animals have allowed to highlight an interesting difference. In this specific
278   case, the effect is more pronounced due to the low expression of the *Thy1* promoter in LIV, and
279   it emphasizes how the shape and the size of the collection volume is defined by the combination
280   of: (i) the influence of the anatomy of the brain region of interest on the photometry field and
281   (ii) the fluorescence distribution across the cell type of interest. This effect is particularly
282   relevant if fiber photometry is applied to animal models of neurodegenerative diseases, such as
283   Alzheimer's disease (AD). In AD models, the presence of amyloid-beta (Aβ) plaques modifies
284   photons propagation beside conventional tissue scattering, as the plaques are associated to
285   higher inhomogeneity of refractive index, higher scattering coefficient, higher birefringence
286   and higher anisotropy of scattering [34–36]. In addition, AD is known to alter connectivity,
287   cellular density and the volumes of specific brain regions [37–40], with our data suggesting
288   that all these parameters play a crucial role in defining the size and shape of fluorescence
289   collection volumes in fiber photometry. Therefore, measuring the photometry efficiency field
290   can be potentially applied to differentiate brain tissue with AD, adding a further source of
291   information to the rapidly evolving field of label-free identification of senile plaques [34].
292   The method employed in this work can be extended to other transgenic mouse lines to
293   identify the actual volumes contributing to the effective functional fluorescence, to better
294   correlate recorded signals and their interpretation within the microcircuits of interest. Recent
295   works have indeed shown how precise targeting of the region(s) and cell type of interests allows
296   dissecting specific neural circuits related to memory, fear and epileptogenic activity, enabling
297   to relate them to specific behavioral activity [41–46]. In the specific case of free-moving mice
298   experiments, we should mention that brain pulsation or animal movements can slightly alter
299   the size and the shape of the photometry efficiency field. This commonly results in fluorescence
300   variations unrelated to the functional signal, usually corrected by adding an isosbestic excitation
301   light to the system [47]. Despite our method does not consider these artifacts in evaluating the
302   collection volumes, it can be applied also on the isosbestic channel, to estimate the overlap of
303   the probed volumes and assess the quality of the implemented artifacts correction. The fiber
304   photometry efficiency fields can be estimated at multiple wavelengths, and they intrinsically
305   account for differences in the scattering parameters as a function of photons' energy. On the
306   other hand, the correction of fast-varying non-functional fluorescence in fiber photometry is

307 still an open question, and it could benefit from Fourier space methods developed in the field
308 of brain imaging [48], that could directly be applied to the image of the output fiber facet.
309 Another aspect to consider when translating the here-reported findings to fresh or living brain
310 tissue is that our experiments are carried in PFA-fixed brain slices. One consequence of this is
311 that hemoglobin absorption, which could represent an additional source of spurious
312 fluorescence, is not considered [49,50]. As well, the PFA fixation itself can set differences on
313 photon propagation, slightly altering scattering parameters and the refractive index [51].

314 The presented data also highlight the limits of flat-cleaved optical fibers to collect photons
315 below the first layers of cortex, and the need of developing complementary methods to achieve
316 this aim. One example on this respect is tapered optical fibers [52], which have shown a more
317 homogeneous signal distribution along a depth of a few millimeters and full compatibility with
318 recently implemented photons detection methods like time-correlated single photon counting
319 for lifetime fluorescence photometry [53]. This also highlights the need for novel technological
320 paradigms for functional fluorescence collection in free-moving mice, able to better match the
321 sensitivity volume with the anatomy of the brain structure of interest.

4. Materials and Methods

4.1 Flat-Cleaved Optical Fibers Fabrication Process

324 We realized flat-cleaved optical fibers stubs from 0.39 NA multimode optical fiber with core
325 and cladding diameters of 200 μm and 225 μm, respectively (Thorlabs FT200UMT). Stubs
326 were cutted with a manual fiber cleaver and connectorized to a 1.25 mm stainless-steel ferrule.
327 The connectorized ends of the fiber stubs were manually polished. Patch fibers were realized
328 from the same fiber type, using a SMA connector on one end and a 1.25 mm stainless-steel
329 ferrule on the other end. Details of the procedure are provided in previous work [9].

4.2 Optical Setup and Specifications

331 The setup used to measure the illumination and the collection fields of an optical fiber is
332 schematically shown in *Figure 1A*. A Pockels cell (Conoptics 350-80-02) is used to modulate
333 the power of a $\lambda_{ex} = 920$ nm fs-pulsed near-infrared (NIR) laser beam (Coherent Chameleon
334 Discovery). A quarter wave plate (Thorlabs AQWP05M-980) converts the linear polarization
335 of the laser beam into circular polarization, and the beam diameter is 5-fold expanded and
336 scanned in the xy plane by using a virtually conjugated galvo pair (Sutter). A 4X/0.28NA
337 objective (Olympus XLFLUOR-340 4x/NA 0.28) is mounted on a z-axis fast piezo focuser
338 (Phisik Instrument P-725.4CD). Fluorescence signal excited into coronal brain slices obtained
339 from *Thy1*-GCaMP6*s* transgenic mice is re-collected by the same objective, routed on a non-
340 descanned collection path through a dichroic mirror (Semrock FF665-Di02), two spherical
341 lenses (Thorlabs LA1708-A and LA1805-A), and a bandpass filter (BPF, Semrock FF01-
342 520/70-25), and detected by a photomultiplier tube (PMT, Hamamatsu H10770PA-40, the
343 "μscope PMT"). The fiber stubs collecting fluorescent light were butt-coupled to a patch fiber
344 and the light back-emitted from the patch fiber was collected by a microscope objective
345 (Olympus Plan N 40x); a BPF (Semrock FF03-525/50-25) select the spectral region of interest
346 and two spherical lenses (Thorlabs LA1050-A and LA1805-A) and a PMT (Hamamatsu
347 H7422P-40, the "fiber PMT"), were used to measure the light intensity. Light emission
348 diagrams at 473 nm (laser light from Laser Quantum Ciel) were imaged with a tube lens
349 (Olympus U-TLU) and a sCMOS camera (Hamamatsu Orca Flash lite 4.0); light emission
350 diagrams were registered over the light collection diagram by rescaling and roto-translation.

4.3 Slices Preparation

352 All experimental manipulations on mice were performed in accordance with protocols
353 approved by Italian Ministry of Health. *Thy1*-GCaMP*s* transgenic mice were anesthetized with
354 isoflurane and were perfused transcardially with 4% paraformaldehyde (PFA) in 0.1 M sodium

355 phosphate buffer. Brains were fixed for 24 h at 4 °C, washed in phosphate buffer saline (PBS)
356 and sectioned (300 μm) coronally using a vibratome (Leica VT1000s). To perform the
357 measurements in the hippocampus and in the striatum, the cerebral cortex and corpus callosum
358 were removed manually with a razor blade.

359 *4.4 Data Analysis*

360 Data analysis was performed with custom written Matlab scripts. Source codes are available
361 from the corresponding author on reasonable request.

362 Briefly, a background subtraction was performed on images acquired by the *fiber* PMT (f)
363 and each slice was divided by the correspondent slice acquired by the *μscope* PMT (μ) to
364 compensate for expression of fluorophore unevenness, obtaining η; the normalized average
365 projection within the depth of focus volume was calculated and the so obtained field was
366 multiplied by the normalized illumination image (β) to obtain ρ. Isosurfaces at 10%, 20%, 40%,
367 60% and 80% were evaluated on a smoothed (smooth window = 11) version of ρ.

368 Histograms reporting feature contributes to the collected signal were evaluated as
369 percentage of the integral over the axial profile of the photometry efficiency fields within the
370 anatomical structure (according to its depth). Error bars represent the standard deviation of the
371 percentages evaluated on different brain slices.

382 **Disclosures.** M.D.V. and F. Pisanello are founders and hold private equity in Optogenix, a company that develops,
383 produces and sells technologies to deliver light into the brain. Tapered fibers commercially available from Optogenix
384 were used as tools in the research. M.P. and Fi.P. have been employed by OptogeniX, a company that develops,
385 produces and sells technologies to deliver light into the brain. MDV: Optogenix srl (I). FP: Optogenix srl (I).

386 **Data availability.** Data underlying the results presented in this paper are available in Ref. [54] and on Zenodo
387 repository by authors after the publication of the paper. Data can also be requested to the authors at any time.

388 **Supplemental document.** See Supplement 1 for supporting content.

389 **References**

390 1. H. Lütcke, "Optical recording of neuronal activity with a genetically-encoded calcium indicator in
391 anesthetized and freely moving mice," Front. Neural Circuits (2010).
392 2. G. Cui, S. B. Jun, X. Jin, G. Luo, M. D. Pham, D. M. Lovinger, S. S. Vogel, and R. M. Costa, "Deep brain
393 optical measurements of cell type–specific neural activity in behaving mice," Nat. Protoc. **9**(6), 1213–1228
394 (2014).
395 3. L. A. Gunaydin, L. Grosenick, J. C. Finkelstein, I. V. Kauvar, L. E. Fenno, A. Adhikari, S. Lammel, J. J.
396 Mirzabekov, R. D. Airan, K. A. Zalocusky, K. M. Tye, P. Anikeeva, R. C. Malenka, and K. Deisseroth,
397 "Natural Neural Projection Dynamics Underlying Social Behavior," Cell **157**(7), 1535–1551 (2014).
398 4. Y. K. Cho, G. Zheng, G. J. Augustine, D. Hochbaum, A. Cohen, T. Knöpfel, F. Pisanello, F. S. Pavone, I.
399 M. Vellekoop, M. J. Booth, S. Hu, J. Zhu, Z. Chen, and Y. Hoshi, "Roadmap on neurophotonics," J. Opt.
400 **18**(9), 093007 (2016).
401 5. Y. Yang, N. Liu, Y. He, Y. Liu, L. Ge, L. Zou, S. Song, W. Xiong, and X. Liu, "Improved calcium sensor
402 GCaMP-X overcomes the calcium channel perturbations induced by the calmodulin in GCaMP," Nat.
403 Commun. **9**(1), 1504 (2018).
404 6. K. D. Piatkevich, S. Bensussen, H. Tseng, S. N. Shroff, V. G. Lopez-Huerta, D. Park, E. E. Jung, O. A.
405 Shemesh, C. Straub, H. J. Gritton, M. F. Romano, E. Costa, B. L. Sabatini, Z. Fu, E. S. Boyden, and X.
406 Han, "Population imaging of neural activity in awake behaving mice," Nature **574**(7778), 413–417 (2019).
407 7. T. Patriarchi, J. R. Cho, K. Merten, M. W. Howe, A. Marley, W.-H. Xiong, R. W. Folk, G. J. Broussard, R.
408 Liang, M. J. Jang, H. Zhong, D. Dombeck, M. von Zastrow, A. Nimmerjahn, V. Gradinaru, J. T. Williams,

409   and L. Tian, "Ultrafast neuronal imaging of dopamine dynamics with designed genetically encoded
410   sensors," Science (80-.). **360**(6396), eaat4422 (2018).
411   8.   S. J. Lee, Y. Chen, B. Lodder, and B. L. Sabatini, "Monitoring Behaviorally Induced Biochemical Changes
412   Using Fluorescence Lifetime Photometry," Front. Neurosci. **13**, (2019).
413   9.   M. Pisanello, F. Pisano, M. Hyun, E. Maglie, A. Balena, M. De Vittorio, B. L. Sabatini, and F. Pisanello,
414   "The Three-Dimensional Signal Collection Field for Fiber Photometry in Brain Tissue," Front. Neurosci.
415   **13**, (2019).
416   10.   D. C. S. Tai, D. A. Hooks, J. D. Harvey, B. H. Smaill, and C. Soeller, "Illumination and fluorescence
417   collection volumes for fiber optic probes in tissue," J. Biomed. Opt. **12**(3), 034033 (2007).
418   11.   F. Zhang, A. M. Aravanis, A. Adamantidis, L. de Lecea, and K. Deisseroth, "Circuit-breakers: optical
419   technologies for probing neural signals and systems," Nat. Rev. Neurosci. **8**(8), 577–581 (2007).
420   12.   G. Yona, N. Meitav, I. Kahn, and S. Shoham, "Realistic Numerical and Analytical Modeling of Light
421   Scattering in Brain Tissue for Optogenetic Applications," eneuro **3**(1), ENEURO.0059-15.2015 (2016).
422   13.   E. Maglie, M. Pisanello, F. Pisano, A. Balena, M. Bianco, B. Spagnolo, L. Sileo, B. L. Sabatini, M. De
423   Vittorio, and F. Pisanello, "Ray tracing models for estimating light collection properties of microstructured
424   tapered optical fibers for optical neural interfaces," Opt. Lett. **45**(14), 3856 (2020).
425   14.   M. A. Tosches and G. Laurent, "Evolution of neuronal identity in the cerebral cortex," Curr. Opin.
426   Neurobiol. **56**, 199–208 (2019).
427   15.   R. Glenn Northcutt and J. H. Kaas, "The emergence and evolution of mammalian neocortex," Trends
428   Neurosci. **18**(9), 373–379 (1995).
429   16.   R. Kötter and K. E. Stephan, "Useless or Helpful? The "Limbic System" Concept," Rev. Neurosci. **8**(2),
430   (1997).
431   17.   A. David and L. Pierre, "Hippocampal Neuroanatomy," in *The Hippocampus Book* (Oxford University,
432   2006), pp. 37–114.
433   18.   A. C. Kreitzer and R. C. Malenka, "Striatal Plasticity and Basal Ganglia Circuit Function," Neuron **60**(4),
434   543–554 (2008).
435   19.   A. Märtin, D. Calvigioni, O. Tzortzi, J. Fuzik, E. Wärnberg, and K. Meletis, "A Spatiomolecular Map of
436   the Striatum," Cell Rep. **29**(13), 4320-4333.e5 (2019).
437   20.   Y. Li, Z. Liu, Q. Guo, and M. Luo, "Long-term Fiber Photometry for Neuroscience Studies," Neurosci.
438   Bull. **35**(3), 425–433 (2019).
439   21.   T.-W. Chen, T. J. Wardill, Y. Sun, S. R. Pulver, S. L. Renninger, A. Baohan, E. R. Schreiter, R. A. Kerr,
440   M. B. Orger, V. Jayaraman, L. L. Looger, K. Svoboda, and D. S. Kim, "Ultrasensitive fluorescent proteins
441   for imaging neuronal activity," Nature **499**(7458), 295–300 (2013).
442   22.   K. S. Girven and D. R. Sparta, "Probing Deep Brain Circuitry: New Advances in in Vivo Calcium
443   Measurement Strategies," ACS Chem. Neurosci. **8**(2), 243–251 (2017).
444   23.   Y. Zhao, S. Araki, J. Wu, T. Teramoto, Y.-F. Chang, M. Nakano, A. S. Abdelfattah, M. Fujiwara, T.
445   Ishihara, T. Nagai, and R. E. Campbell, "An Expanded Palette of Genetically Encoded Ca2+ Indicators,"
446   Science (80-.). **333**(6051), 1888–1891 (2011).
447   24.   G. Feng, R. H. Mellor, M. Bernstein, C. Keller-Peck, Q. T. Nguyen, M. Wallace, J. M. Nerbonne, J. W.
448   Lichtman, and J. R. Sanes, "Imaging Neuronal Subsets in Transgenic Mice Expressing Multiple Spectral
449   Variants of GFP," Neuron **28**(1), 41–51 (2000).
450   25.   Nikon's MicroscopyU, "Depth of Field and Depth of Focus," (2021),
451   https://www.microscopyu.com/microscopy-basics/depth-of-field-and-depth-of-focus.
452   26.   C. J. Engelbrecht, W. Göbel, and F. Helmchen, "Enhanced fluorescence signal in nonlinear microscopy
453   through supplementary fiber-optic light collection," Opt. Express **17**(8), 6421 (2009).
454   27.   H. Dana, T.-W. Chen, A. Hu, B. C. Shields, C. Guo, L. L. Looger, D. S. Kim, and K. Svoboda, "Thy1-
455   GCaMP6 Transgenic Mice for Neuronal Population Imaging In Vivo," PLoS One **9**(9), e108697 (2014).
456   28.   J. L. Lanciego, N. Luquin, and J. A. Obeso, "Functional Neuroanatomy of the Basal Ganglia," Cold Spring
457   Harb. Perspect. Med. **2**(12), a009621–a009621 (2012).
458   29.   A. Peters and D. A. Kara, "The neuronal composition of area 17 of rat visual cortex. I. The pyramidal
459   cells," J. Comp. Neurol. **234**(2), 218–241 (1985).
460   30.   F. Scala, D. Kobak, S. Shan, Y. Bernaerts, S. Laturnus, C. R. Cadwell, L. Hartmanis, E. Froudarakis, J. R.
461   Castro, Z. H. Tan, S. Papadopoulos, S. S. Patel, R. Sandberg, P. Berens, X. Jiang, and A. S. Tolias, "Layer
462   4 of mouse neocortex differs in cell types and circuit organization between sensory areas," Nat. Commun.
463   **10**(1), 4174 (2019).
464   31.   A. N. Yaroslavsky, P. C. Schulze, I. V Yaroslavsky, R. Schober, F. Ulrich, and H.-J. Schwarzmaier,
465   "Optical properties of selected native and coagulated human brain tissues in vitro in the visible and near
466   infrared spectral range," Phys. Med. Biol. **47**(12), 305 (2002).
467   32.   J. Sun, S. J. Lee, L. Wu, M. Sarntinoranont, and H. Xie, "Refractive index measurement of acute rat brain
468   tissue slices using optical coherence tomography," Opt. Express **20**(2), 1084 (2012).
469   33.   S. I. Al-Juboori, A. Dondzillo, E. A. Stubblefield, G. Felsen, T. C. Lei, and A. Klug, "Light Scattering
470   Properties Vary across Different Regions of the Adult Mouse Brain," PLoS One **8**(7), e67626 (2013).
471   34.   M. Borovkova, A. Bykov, A. Popov, A. Pierangelo, T. Novikova, J. Pahnke, and I. Meglinski, "Evaluating
472   β-amyloidosis progression in Alzheimer's disease with Mueller polarimetry," Biomed. Opt. Express **11**(8),
473   4509 (2020).

35. B. Baumann, A. Woehrer, G. Ricken, M. Augustin, C. Mitter, M. Pircher, G. G. Kovacs, and C. K. Hitzenberger, "Visualization of neuritic plaques in Alzheimer's disease by polarization-sensitive optical coherence microscopy," Sci. Rep. **7**(1), 43477 (2017).

36. M. Lee, E. Lee, J. Jung, H. Yu, K. Kim, J. Yoon, S. Lee, Y. Jeong, and Y. Park, "Label-free optical quantification of structural alterations in Alzheimer's disease," Sci. Rep. **6**(1), 31034 (2016).

37. N. P. Oxtoby, S. Garbarino, N. C. Firth, J. D. Warren, J. M. Schott, and D. C. Alexander, "Data-Driven Sequence of Changes to Anatomical Brain Connectivity in Sporadic Alzheimer's Disease," Front. Neurol. **8**, (2017).

38. H. Fu, J. Hardy, and K. E. Duff, "Selective vulnerability in neurodegenerative diseases," Nat. Neurosci. **21**(10), 1350–1358 (2018).

39. V. N. Nikolenko, N. A. Rizaeva, N. M. Beeraka, M. V. Oganesyan, V. A. Kudryashova, A. A. Dubovets, I. D. Borminskaya, K. V. Bulygin, M. Y. Sinelnikov, and G. Aliev, "The mystery of claustral neural circuits and recent updates on its role in neurodegenerative pathology," Behav. Brain Funct. **17**(1), 8 (2021).

40. Y. Ying and J.-Z. Wang, "Illuminating Neural Circuits in Alzheimer's Disease," Neurosci. Bull. **37**(8), 1203–1217 (2021).

41. X. Dong, X. Zhang, F. Wang, N. Liu, A. Liu, Y. Li, L. Wei, F. Chen, S. Yuan, K. Zhang, S. Hou, Q. Jiao, Q. Hu, C. Guo, T. Wu, S. Wei, and H. Shen, "Simultaneous calcium recordings of hippocampal CA1 and primary motor cortex M1 and their relations to behavioral activities in freely moving epileptic mice," Exp. Brain Res. **238**(6), 1479–1488 (2020).

42. X. Zhang, Z. Qiao, N. Liu, L. Gao, L. Wei, A. Liu, Z. Ma, F. Wang, S. Hou, J. Li, and H. Shen, "Stereotypical patterns of epileptiform calcium signal in hippocampal CA1, CA3, dentate gyrus and entorhinal cortex in freely moving mice," Sci. Rep. **9**(1), 4518 (2019).

43. S. Pan, S. R. Mayoral, H. S. Choi, J. R. Chan, and M. A. Kheirbek, "Preservation of a remote fear memory requires new myelin formation," Nat. Neurosci. **23**(4), 487–499 (2020).

44. H. Qin, L. Fu, B. Hu, X. Liao, J. Lu, W. He, S. Liang, K. Zhang, R. Li, J. Yao, J. Yan, H. Chen, H. Jia, B. Zott, A. Konnerth, and X. Chen, "A Visual-Cue-Dependent Memory Circuit for Place Navigation," Neuron **99**(1), 47-55.e4 (2018).

45. Q. Guo, J. Zhou, Q. Feng, R. Lin, H. Gong, Q. Luo, S. Zeng, M. Luo, and L. Fu, "Multi-channel fiber photometry for population neuronal activity recording," Biomed. Opt. Express **6**(10), 3919 (2015).

46. Y. Wang, E. M. DeMarco, L. S. Witzel, and J. D. Keighron, "A selected review of recent advances in the study of neuronal circuits using fiber photometry," Pharmacol. Biochem. Behav. **201**, 173113 (2021).

47. T. Akam and M. E. Walton, "pyPhotometry: Open source Python based hardware and software for fiber photometry data acquisition," Sci. Rep. **9**(1), 3521 (2019).

48. G. Molodij, A. Sdobnov, Y. Kuznetsov, A. Harmelin, I. Meglinski, and V. Kalchenko, "Time-space Fourier $\kappa \omega'$ filter for motion artifacts compensation during transcranial fluorescence brain imaging," Phys. Med. Biol. **65**(7), 075007 (2020).

49. W. Zheng, D. Li, Y. Zeng, Y. Luo, and J. Y. Qu, "Two-photon excited hemoglobin fluorescence," Biomed. Opt. Express **2**(1), 71 (2011).

50. E. A. Shirshin, B. P. Yakimov, S. A. Rodionov, N. P. Omelyanenko, A. V Priezzhev, V. V Fadeev, J. Lademann, and M. E. Darvin, "Formation of hemoglobin photoproduct is responsible for two-photon and single photon-excited fluorescence of red blood cells," Laser Phys. Lett. **15**(7), 075604 (2018).

51. A. Pitzschke, B. Lovisa, O. Seydoux, M. Haenggi, M. F. Oertel, M. Zellweger, Y. Tardy, and G. Wagnières, "Optical properties of rabbit brain in the red and near-infrared: changes observed under in vivo, postmortem, frozen, and formalin-fixated conditions," J. Biomed. Opt. **20**(2), 025006 (2015).

52. F. Pisano, M. Pisanello, S. J. Lee, J. Lee, E. Maglie, A. Balena, L. Sileo, B. Spagnolo, M. Bianco, M. Hyun, M. De Vittorio, B. L. Sabatini, and F. Pisanello, "Depth-resolved fiber photometry with a single tapered optical fiber implant," Nat. Methods **16**(11), 1185–1192 (2019).

53. M. Bianco, A. Balena, M. Pisanello, F. Pisano, L. Sileo, B. Spagnolo, C. Montinaro, B. L. Sabatini, M. De Vittorio, and F. Pisanello, "Comparative study of autofluorescence in flat and tapered optical fibers towards application in depth-resolved fluorescence lifetime photometry in brain tissue," Biomed. Opt. Express **12**(2), 993 (2021).

54. Data availability (2021), https://cbn.iit.it/openfiberphotometry.